Shape-controlled self-assembly of light-powered microrobots into ordered microchains for cells transport and water remediation

Xia Peng[1], Mario Urso[1], Martina, Ussia[1], Martin Pumera[1, 2, 3, 4 *]

[1] Future Energy and Innovation Laboratory, Central European Institute of Technology, Brno University of Technology, Purkynova 123, 61200, Brno, Czech Republic

[2] Center for Nanorobotics and Machine Intelligence, Department of Chemistry and Biochemistry, Mendel University in Brno, Zemedelska 1, 61300, Brno, Czech Republic

[3] Department of Medical Research, China Medical University Hospital, China Medical University, No. 91 Hsueh-Shih Road, Taichung, Taiwan

[4] Department of Chemical and Biomolecular Engineering, Yonsei University, 50 Yonsei-ro, Seodaemun-gu, 03722, Seoul, Korea

* Corresponding author e-mail: martin.pumera@ceitec.vutbr.cz

Keywords: micromotors; swarming; collective behavior; self-assembly; cargo transport; photo-Fenton degradation.

Abstract

Nature presents spectacular collective behavior aiming to accomplish complex tasks, inspiring the development of cooperative micro/nanorobots. Herein, the spontaneous assembly of hematite-based microrobots with different shapes is presented. Autonomous motile light-driven hematite/Pt microrobots with cubic and walnut shapes are prepared by hydrothermal synthesis, followed by the deposition of a Pt layer to design Janus structures. Both microrobots show a fuel-free motion ability under light irradiation. Because of the asymmetric orientation of the dipolar moment in the crystal, cubic hematite/Pt microrobots can self-organize into ordered microchains, contrary to the random aggregation observed for walnut-like microrobots. The microchains exhibit different synchronized motions under light irradiation depending on the mutual orientation of the individual microrobots during the assembly, which allow them to accomplish multiple tasks, including capturing, picking up and transporting microscale objects, such as yeast cells and suspended matter in water extracted from personal care products, as well as degrading polymeric materials. Such light-powered self-assembled microchains demonstrate an innovative cooperative behavior for small-scale multitasking artificial robotic systems, holding great potential toward cargo capture, transport and delivery, and wastewater remediation.

Introduction

Ranging from ant colonies to bird flocking, nature provides a plethora of intriguing collective phenomena in biological systems, self-organized in a synchronized manner to accomplish desired tasks and goals that individual capabilities cannot achieve. For example, a colony of ants can cooperate based on achievable local information to transport food, construct nests, and self-assemble into sophisticated structures when encountering rugged terrain;[1] vast groups of starlings can twist, turn, swoop and swirl across the sky in beautiful shape-shifting clouds, known as starling murmuration, to scare and repel natural enemies. Such ingenious behaviors in the absence of any controllers exhibit superior advantages to complete tasks in a highly efficient and robust way, or survive in complex environments, fascinating researchers especially from the field of micro/nanorobotics. Inspired by the cooperative actions of living organisms, various artificial swarm robotic systems consisting of relatively simple robots have been developed, capable of complex task sequencing and communal formations relying on operator inputs or artificial intelligent software.[2, 3]

Artificial micro/nanorobots, a relatively young field of research that has seen remarkable growth, becoming one of the most attractive research topics nowadays, are autonomously self-propelled micro/nanomaterials able to harvest and convert energy from their surrounding environment into autonomous movement.[4, 5] Various energy sources, including chemical fuels (H_2O_2, glucose, urea) or external stimuli such as light, magnetic fields, and ultrasound, have been exploited to activate the self-propulsion of micro/nanorobots.[6–13] Particularly, light is a very attractive energy source to power microrobots because it is powerful, renewable, and abundant. To obtain an active moving particle, it is necessary to have an asymmetric structure, which in turn converts this asymmetry into motion.[14, 15] In this regard, the “two-faced” Janus microrobots consisting of a photocatalytic semiconductor (UV-light-activated TiO_2 and ZnO, visible light-activated Fe_2O_3 and BiOI) asymmetrically covered by a metal layer (Pt, Au, Ag) represent the most efficient light-powered self-motile microrobots.[16–25] Owing to their powerful motion, micro/nanorobots can accomplish numerous and different tasks, holding excellent prospects in various application fields from biomedicine to environmental remediation and sensing.[26–29] Still, further improvements are expected from rudimentary communication between individual microrobots (e.g. micro/nanorobotic swarms), allowing synchronized operation and high adaptability to different complex conditions. Based on this consideration, the careful selection of the constituent materials plays a crucial role in micro/nanorobots' organization manners. In fact, self-propelled micro/nanorobots composed of colloids can exhibit swarm behaviors via physical or chemical interactions, such as dipole–dipole interactions, capillary forces, van der Waals forces, *etc.*, rather than informatic communication in macrorobotic systems.[30–36] Nevertheless, the influence of micro/nanorobots' shape on their coordination is still not investigated. In addition, self-assembled microrobots that mimic the collective behavior of the living systems without any controllers remain challenging.

In this work, we demonstrate how the shape of the microrobots can influence their collective behaviors using cubic and walnut-shaped light-powered hematite/Pt Janus microrobots (Scheme 1). The microrobots were fabricated by asymmetrically depositing a 30 nm thin Pt layer on the surface of walnut and cubic-shaped hematite microparticles synthesized by facile and low-cost hydrothermal processes. All microrobots show self-propulsion under UV-light irradiation in pure water. Cubic microrobots display faster locomotion than walnut ones, agreeing with the larger mixed potential differences observed from Tafel measurements. Moreover, cubic hematite microrobots can self-assemble into impressive microchains exhibiting three types of autonomous motion under UV-light irradiation, according to the orientation of microrobots during the formation of the microchains. The self-assembled microchains can address multitasking requirements when encountering environmental variations including capturing, picking up and transporting micro-objects, such as cells and suspended matter in water resulting from the contamination with personal care products, as well as photocatalytic degradation of polymer chains. This work provides novel self-assembled light-powered microchains based on dipolar interactions between individual cubic hematite/Pt Janus microrobot, which hold promise cargo transportation and degradation of pollutants in water, including plastic materials.

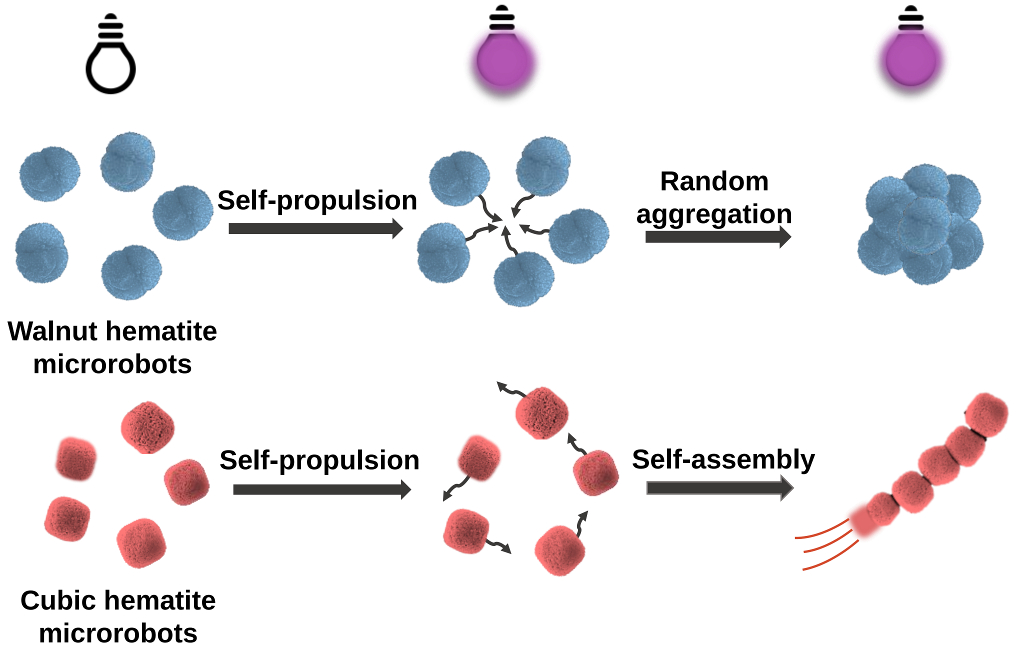

Scheme 1. Shape-controlled self-assembly capabilities of light-powered hematite/Pt Janus microrobots under UV-light irradiation.

Experimental section

Synthesis of walnut-shaped hematite microparticles: Walnut hematite microparticles were prepared by a one-step hydrothermal reaction. In brief, 1 M $FeCl_3$ (Alfa Aesar, 98%) was added to deionized water (DI water, 18 MΩ cm) to form a homogeneous solution under magnetic stirring. Then the solution was transferred into a 50 mL Teflon-lined stainless-steel autoclave, heated at 160°C for 20 h, and cooled to room temperature naturally. Afterward, the product was collected by centrifugation and washed several times with DI water and ethanol. Finally, it was dried in a vacuum oven at 60°C for 12 h.

Synthesis of cubic-shaped hematite microparticles: In a typical synthesis, 0.5 M $FeCl_3$ (Alfa Aesar, 98%) and 1.2 g hexamethylenetetramine (Sigma Aldrich, 99.5%) were directly dissolved in a 30 mL mixture of ethanol and DI water (1:1 v/v) with vigorous magnetic stirring. Subsequently, 3wt% of $CuCl_3$ (Alfa Aesar, 98%) was added to the above solution. After 30 min stirring, the mixture was transferred into a Teflon-lined stainless-steel autoclave and heated at 160℃ for 12 h. After that, the autoclave was cooled naturally down to room temperature. The resultant precipitate was collected by centrifugation, washed several times with DI water and ethanol, and then dried at 80°C in a vacuum oven for 8h.

Preparation of hematite/Pt Janus microrobots: The synthesized hematite microparticles were suspended in DI water (5 mg mL^{-1}) and dispersed by sonication. The suspension was dropped by a pipette on glass slides and dried overnight. A 30 nm thin Pt layer was asymmetrically deposited on hematite microparticles by the sputtering method. The real-time thickness of the sputtered Pt layer was controlled by a quartz crystal microbalance. After the sputtering process, microrobots were released using a scalpel.

Microrobots morphological, chemical and structural characterization: Scanning electron microscopy (SEM) images of hematite microparticles and hematite/Pt Janus microrobots were obtained with a Tescan MIRA 3 XMU instrument. Energy-dispersive X-ray spectroscopy (EDX) mapping analysis was performed using an Oxford EDX detector connected to the SEM. The XRD patterns of the products were examined by a Rigaku SmartLab 3kW diffractometer, equipped with a fine focus Cu sealed tube operating at 40 kV and 30 mA.

Motion experiments: A Nikon ECLIPSE TS2R inverted microscope coupled with a Basler digital camera acA1920-155uc was used to record the microrobots' motion. Briefly, a microrobot aqueous suspension was dropped on a glass slide. Different concentrations of H_2O_2 (Merck, 30%) were subsequently added to the drop to study microrobot motion in 0, 0.1, and 1% H_2O_2. All experiments were carried out in the absence of surfactants. Then, the microrobots were activated by a 365 nm UV LED (Cool LED pE-100) operated at a measured light intensity of 1.6 W cm^{-2}. Videos were recorded at 20 fps and analyzed to obtain microrobot tracks and calculate their speed through NIS Elements Advanced Research software.

Electrochemical measurements: Tafel experiments were carried out using a customized photoelectrochemical setup with a 365 nm UV LED (700 mA powered LZ4-04UV00, LedEngin Inc.) in the two-electrode configuration with either hematite electrode or Pt electrode as working electrodes and an Ag/AgCl electrode as both the reference and counter electrode. The hematite working electrode was made by dropping 100 μL of a 5 mg mL^{-1} aqueous suspension of walnut or cubic hematite microparticles on commercial ITO-covered glass slides (1 x 2 cm^2, Sigma Aldrich, 8–12 Ω sq^{-1}), and overnight drying. Pt working electrode was obtained by sputtering a 30 nm thin Pt layer on an ITO-covered glass slide. Tafel measurements were recorded at a scan rate of 5 mV s^{-1} from -0.2 to 0.6 V *vs.* Ag/AgCl under UV-light irradiation on the working electrodes (1 x 1 cm^2 immersed area) in DI water using a Metrohm AUTOLAB potentiostat.

Numerical simulation

The numerical simulation was performed using the transport of diluted species module of the COMSOL Multiphysics software for the cross-section of two adjacent hematite/Pt Janus microrobots. Each microrobot was designed as a square with a size of 2 μm x 2 μm. The H_2O generation at the interface between Pt and H_2O_2 due to the photogenerated electron-hole pairs in hematite was simulated. For this purpose, one of the side of each square was considered as the generation one to emulate the face of the microrobot coated by the Pt layer. The most significant configurations of the two microrobots have been taken into account in the simulation. To calculate the H_2O diffusion for 0.1 s light irradiation, an H_2O diffusion coefficient in water at 25°C of 2.99×10^{-9} m^2 s^{-1} was used, while the photogeneration rate was set to 1 mmol m^{-2} s^{-1}.

Yeast cells transport: 5 g of commercial yeast was suspended in 200 ml of distilled water under magnetic stirring for 10 min. Then, the solution was moved to an autoclave and heated at 121°C for 15 min. After that, the broth was vortexed briefly to disperse yeast cells and immediately moved to a temperature-controlled shaking incubator at 300 rpm for 4 hours at 37°C. Yeast cells were centrifuged at 5000 rpm for 5 min to remove the culture media and then transferred in DI water. An aqueous diluted yeast suspension (5 μL) and a suspension of the cubic hematite microrobots (5 μL, 1 mg mL^{-1}) were placed onto a glass slide to record the videos at a final concentration of 0.1% H_2O_2.

Removal of suspended matter in water: 1 g of commercial toothpaste was dissolved in 200 ml water. Then, a vacuum filtration device was used to filter the solution. A membrane (Whatman membrane filter) with 0.2 μm holes was used. After the filtration, the extracts were washed with distilled water three times. The final products were obtained after drying in a vacuum oven for 5 h. For the removal of suspended matter, 5 μL of the resulting solution (2 mg mL^{-1}), 5 μL cubic hematite microrobots (3 mg mL^{-1}), and 5 μL 0.1% H_2O_2 (the final concentration) were mixed to a clean glass slide to record videos.

PEG photodegradation: The photocatalytic degradation ability of microrobots was evaluated through the degradation of polyethylene glycol (PEG, Mw 4000, Alfa Aesar) under UV-light irradiation. 1 mg of PEG 4000 and 1 mg of microrobots (3 mg mL^{-1})were added to 1 ml of 1 % H_2O_2 solution in a disposable cuvette. The cuvette was irradiated for 24 h using a 365 nm UV LED lamp (9 W) as the light source. After the photocatalytic experiments, the solution was centrifugated at 3500 rpm for 5 min to separate the solution from the microrobots for further analyses. The PEG 4000 degradation was evaluated by UltrafleXtreme Matrix-Assisted Laser Desorption/Ionization Mass Spectrometry (MALDI-MS, Bruker Daltonics, Bremen, Germany) operated in linear positive detection mode following the protocol of a previous paper. [22]

Results and discussion

Janus Microrobots Fabrication

Active interactions between individual microrobots are important for studying emergent phenomena. In this work, we investigated the influence of microrobots' shape on their collective behavior using self-propelled light-driven walnut and cubic hematite/Pt Janus microrobots.

As illustrated in **Figure 1a**, different shapes of hematite microparticles were first synthesized by facile hydrothermal reactions. To fabricate Janus microrobots, 30 nm Pt films were physically deposited on the surface of hematite microparticles by the sputtering method. Scanning electron microscopy (SEM) images and the corresponding elemental mapping images obtained by energy-dispersive X-ray spectroscopy (EDX) of the two hematite shapes are presented in **Figures 1b and c**. **Figure 1b** shows walnut hematite microparticles with a diameter of 2–3 μm and a hierarchical porous structure resulting from the random arrangement of hematite nanoparticles (appromaximately 100 nm). **Figure 1c** displays instead cubic hematite microparticles with a size of approximately 2 μm. In this case, the cubic shape results from the ordered assembly of hematite nanoparticles (appromaximately 50 nm). EDX images manifest a uniform distribution of Fe and O for both hematite microparticles. After Pt layer deposition, both hematite microrobots exhibit the distinct asymmetrical structure of Janus microrobots, as indicated by the uneven Pt distribution.

X-ray diffraction (XRD) was carried out to assess hematite microparticles crystalline structure, as shown in **Figure S1**. The recorded XRD patterns correspond to the characteristic α-Fe_2O_3 pattern (PDF card # 00-001-1053). The peaks appearing at the following 2θ values ≈24.12°, 33.12°, 35.61°, 40.88°, 49.51°, 54.22°, 57.63°, 62.45°, and 64.11°, corresponds to (012), (104), (110), (113), (024), (116), (018), (214), and (300) planes, respectively. These peaks agree with the distinctive rhombohedral centered hexagonal structure of the α-Fe_2O_3 crystal, commonly called hematite.[22]

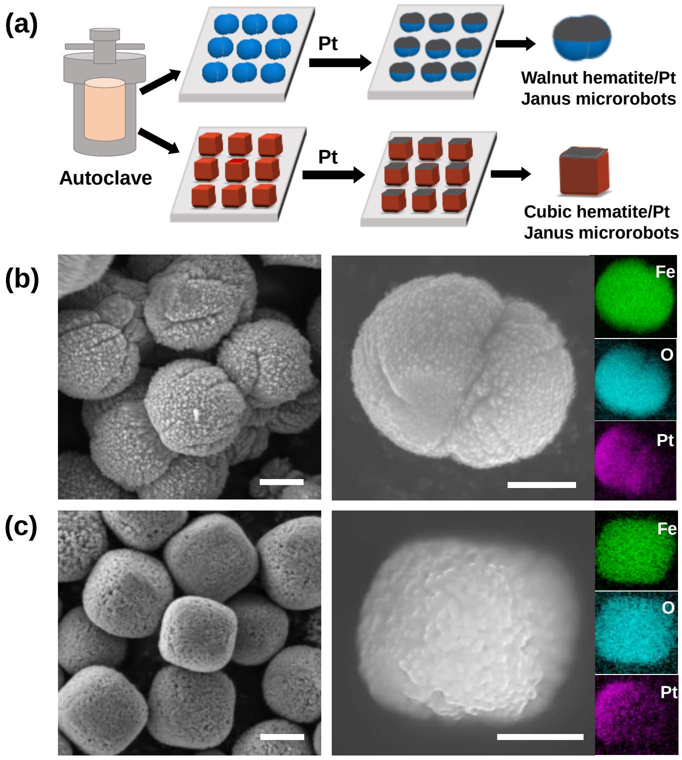

Figure 1. (a) Fabrication scheme of hematite/Pt Janus microrobots with different shapes. SEM and EDX elemental mapping images of (b) walnut and (c) cubic hematite/Pt Janus microrobots (scale bars are 1 μm).

Single Microrobots Propulsion

The hematite/Pt Janus microrobots displayed autonomous self-propelled abilities in water and minor amounts of H_2O_2 fuel when irradiated with UV-light based on a light-induced self-electrophoretic mechanism, as shown previously.[29]. **Figure 2a** reports the speed of the walnut and cubic microrobots in different concentrations of H_2O_2, calculated from the average of more than 10 different microrobots. In pure water (0% H_2O_2), the speed of walnut microrobots (5 ± 1 μm s^{-1}) is slightly higher than cubic hematite microrobots (4.2 ± 0.8 μm s^{-1}). However, the addition of a small amount of H_2O_2 (0.1%) results in a huge increase in the speed of cubic hematite microrobots (19 ± 1 μm s^{-1}), while the speed of walnut ones is merely 6 ± 1 μm s^{-1}. **Figure 2b** shows the trajectories of walnut and cubic microrobots in 0.1% H_2O_2 under UV-light irradiation after 5 s recording, which demonstrate the much longer navigation within 5 s of the cubic ones (**Supplementary Movie 1**). When a higher concentration of H_2O_2 was applied (1% H_2O_2), there is an eight-fold increase in the speed of cubic microrobots (32 ± 3 μm s^{-1}) compared to pure water, while it is just tripled for walnut ones (14 ± 2 μm s^{-1}).

To better understand the underlying reasons for the differences in the speed of microrobots with different shapes, the mixed potential difference between walnut and cubic hematite microparticles and a Pt electrode was evaluated in 1% H_2O_2 under UV-light irradiation. According to previous reports, it has been demonstrated that the larger is such potential difference, the higher is the speed.[22, 25] The measured Tafel plots are shown in **Figure 2c**. The potential difference between cubic hematite microparticles and Pt electrodes (47 mV) is much larger compared to walnut hematite (4 mV), consistently with the trend of microrobots' speed in **Figure 2a.**

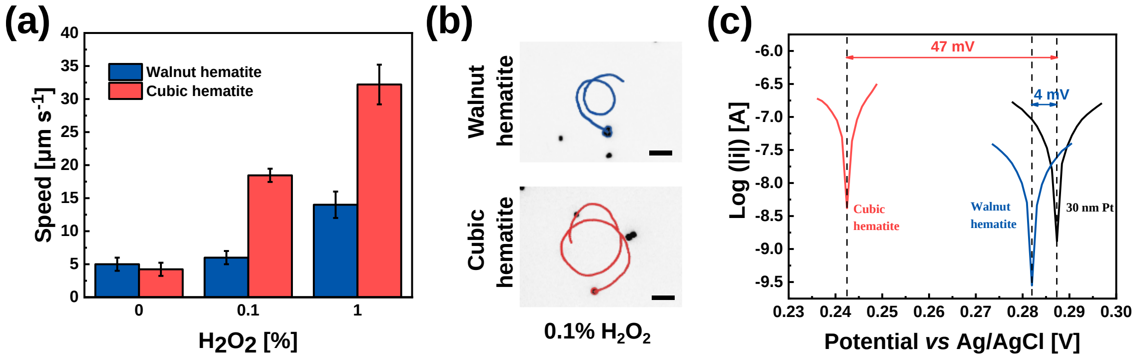

Figure 2. (a) Comparison of microrobots' speed in pure water and in different concentrations of H_2O_2. (b) Micrographs showing walnut and cubic microrobots trajectories in 0.1% H_2O_2 under UV-light irradiation (scale bars are 5 μm). (c) Tafel plots of walnut and cubic hematite electrodes and 30 nm Pt electrode in 1% H_2O_2 under UV-light irradiation.

Collective Behaviour of Self-Assembled Microchains

We discovered that different microrobots' shapes give rise to different interactions. **Figure 3a** displays the temporal evolution of systems of walnut and cubic microrobots. In the beginning, walnut and cubic microrobots are randomly dispersed in water. After 10 min of observation, walnut microrobots display a random aggregation into large disordered clusters. On the contrary, cubic microrobots self-organize into ordered microchains, which can be observed from both optical microscopy and SEM. The live formation of the microchains is presented also in the **Supplementary Movie 2**, while several other microchains are reported in **Figure S2**. This intriguing phenomenon is due to the orientation of the dipolar moment in the crystal of cubic hematite, as illustrated **in Figure 3b**.[37] For cubic hematite, the dipolar moment is not aligned along a particle symmetry axis. Moreover, cubic hematite displays a fixed and permanent dipolar moment, even in the absence of a magnetic field, which is strong enough to induce the formation of self-assembled microchains.[38] It is worth noting that the presence of the Pt layer does not influence the active interaction between individual hematite microrobots, also as shown in **Figure S2**. The length of the self-assembled microchains was measured both in dark and under UV-light irradiation and plotted as a function of the time, finding that it increases from 20 ± 3 μm to 100 ± 20 μm in dark and from 18 ± 4 μm to 80 ± 16 μm in the presence of UV-light when the time changes from 5 to 20 min (**Figure 3c**). We assumed that the light-induced motion of microrobots influence the formation of microchains to a certin degree, leading to shorter length under light irradiation.

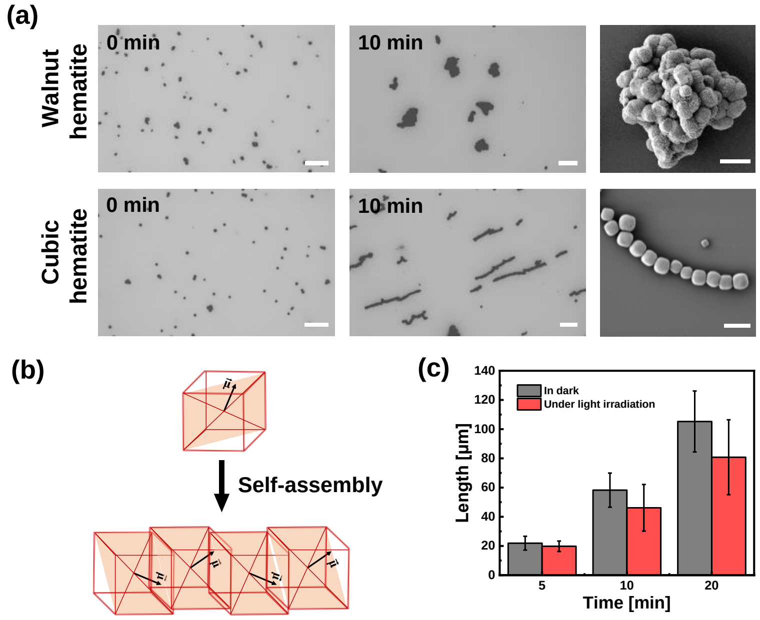

Figure 3. (a) Self-assembly of walnut and cubic microrobots in pure water in the absence of UV-light irradiation, and the corresponding SEM images after 10 min of observation (scale bars for SEM are 5 μm). (b) Dipolar moment orientation in a hematite cube and the alignment of a chain. (c) Length of the self-assembled microchains formed in pure water in the absence and presence of UV-light irradiation

as a function of time.

The motion of the self-assembled microchains under UV-light irradiation was then investigated. The microchains exhibit three main motion modes in 0.1% H_2O_2 under UV-light irradiation, associated with a self-propulsion direction that is (1) parallel or (2) perpendicular to the microchain axis, or (3) a rotational behavior (**Supplementary Movie 3**). **Figure 4a** presents a series of time-lapse images, which illustrate the autonomous locomotion of microchains with the different propulsion modes.

The peculiar and varying motility of the microchains is ascribed to the distribution of the microrobots' Pt layers along the microchains, which depends on the microrobots' mutual orientation during the self-assembly process. To corroborate this hyphotesis, a numerical simulation of the 2D spatial distribution of H_2O resulting from the reaction between H_2O_2 and the photogenerated electrons transferred from hematite to Pt was conducted. In fact, this simulation provides an idea of the product spatial gradient which is responsible for microchains' self-propulsion. To simplify the calculation, a microchain formed by only two adjacent microrobots was considered. The different orientations of the Pt layer in the two microrobots give rise to different configurations, as shown in Figure 4(b). In the configuration n. 1 and 2, the Pt layers are on the small side of the microchains. However, the configuration n. 1 results in the movement of the microchains along its axis, while the configuration n. 2 leads to a static microchain as the driving forces of the two microrobots are equal and oppositively directed. The configurations n. 3 and 4 are a combination of translation and rotation, while configuration n. 5 is responsible for the pure rotation of the microchain. Finally, the configuration n. 6 where the two Pt layer are adjacent and placed on the longer lateral side of the microchain enables the locomotion of the microchain along the direction perpendicular to its axis.

Such emerging collective behavior, leading to a synchronized motion of the microchains, is promising for completing tasks like the transport of cells or suspended matter as an example of possible contamination in water.

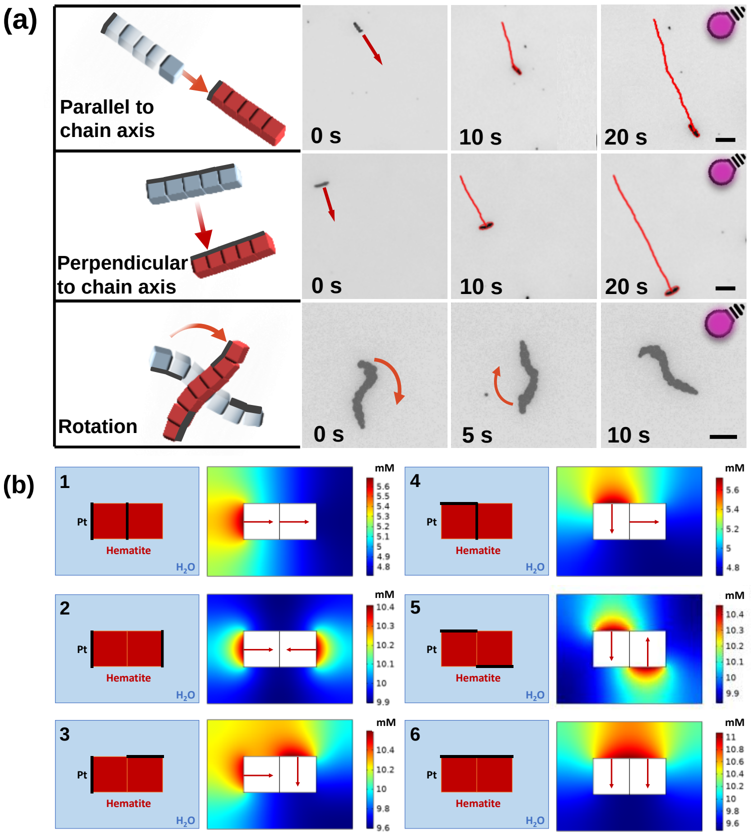

Figure 4. (a) Different motion modes of self-assembled microchains formed by cubic microrobots in 0.1% H_2O_2 under UV-light irradiation (scale bars are 5 μm). (b) Simulation of 2D spatial distribution of H_2O resulting from the reaction between H_2O_2 and the photogenerated electrons transferred from hematite to Pt for different configurations of a 2-microrobots microchain. The arrows indicate the direction of the driving force.

Yeast cells capture, transport and release

Light-driven microrobots have demonstrated diverse interactions with surrounding passive particles, which is of great importance for performing desirable tasks such as cargo transport, objects manipulation, and sensing. [39] The self-assembly of cubic microrobots into autonomous motile microchains inspired their use for cargo transport application using yeast cells as a model for living microorganisms, owing to their relatively big size (approximately 2-3 μm for haploids) that can be easily visualized by optical microscopy. **Figure 5** displays the interaction between a cubic microrobot and yeast cells under UV-light irradiation in 0.1% H_2O_2 (**Supplementary Movie 4, 5**). The time-lapse images in **Figure 5a** demonstrate the long-distance transportation of a yeast cell by a single cubic microrobot. Besides, the rotation of multiple yeast cells can be realized by a single microrobot, as shown in **Figure 5b**. The transportation capability of self-assembled microchains were also evaluated. The self-assembled microchain in **Figure 5c** shows an autonomous motion parallel to the microchain axis, capturing four yeast cells, proving how the cooperation of several microbots allows capturing and transporting several cells simultaneously. We further investigated the controlled release of yeast cells by switching on/off the UV-light in 0.1% H_2O_2 using the self-assembled microchains. As illustrated in **Figure 5d,** the microchain captured one yeast cell under UV-light irradiation. By turning off the UV-light, the yeast cell was immediately released, which is attributed to the hindered self-propulsion of the microchain and consequently the stopped generation of a chemical gradient around it. When UV-light has turned on again, the microchain picked up again the yeast cell and continued to transport it.

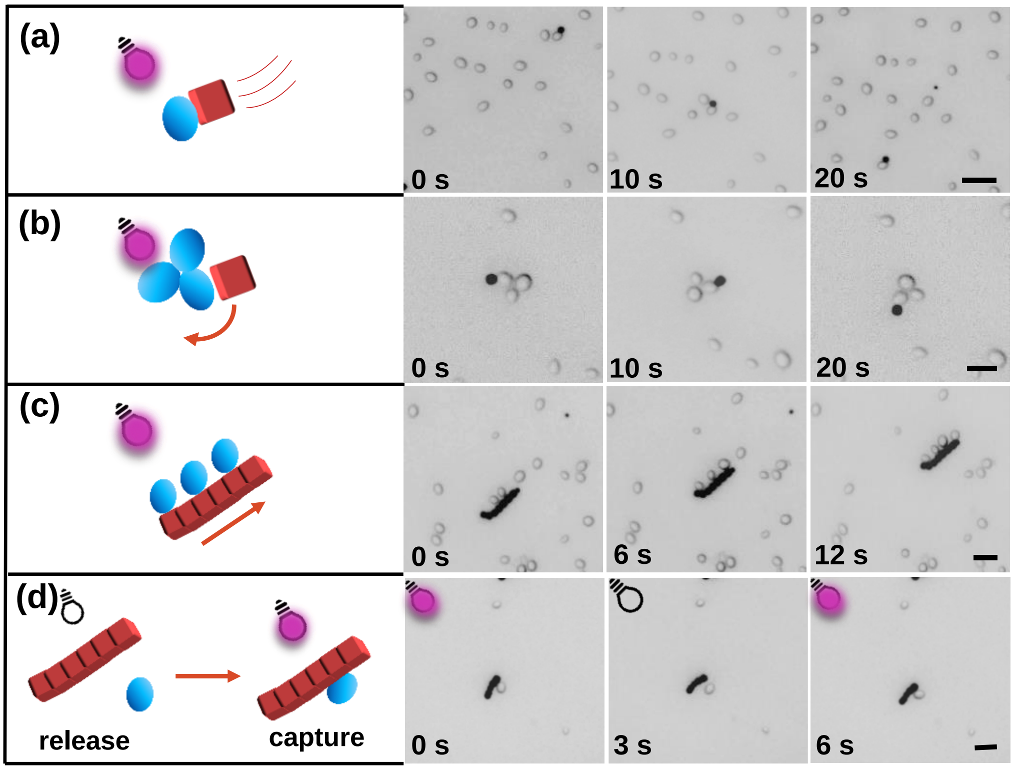

Figure 5. Interaction of cubic microrobots and self-assembled microchains with yeast cells in 0.1% H_2O_2 under UV-light irradiation. Time-lapse images of (a) a single microrobot transporting a yeast cell and (b) a single microrobot rotating with yeast cells, (c) a microchain capturing multiple yeast cells, and (d) controlled capture/release of the yeast cell by a microchain by turning on/off the UV-light (scale bars are 5 µm).

Removal of suspended matters in water

Autonomous moving self-assembled microchains composed of synchronized microrobots open a new opportunity to separate microplastics and suspended matter from water. The removal of suspended matter (**Figure S3**) extracted from commercial toothpaste was accomplished by the shoveling effect of microchains under UV-light irradiation in 0.1% H_2O_2 (**Supplementary Movie 6**). The artificially colored time-lapse images in **Figure 6a** (original images in **Figure S4**) demonstrate the motion of a microchain that is cleaning water by collecting suspended matter “on-the-fly.” In fact, it can be observed that the removal area increases along the propulsion trajectory of the microchain, and within 60 s, a considerable number of pieces were quantitively accumulated on the forward side of the microchain, which further proves robust binding force between the single microrobots of the microchain. Hematite intrinsic magnetism can be used to navigate the microchains with captured microplastics using an external magnetic field, completing the remediation process.

PEG photodegradation

To demonstrate the ability of the self-assembled microchains to degrade pollutants in water, the PEG 4000 has been chosen as a model for polymeric materials like plastics whose degradation can be monitored by Matrix-Assisted Laser Desorption/Ionization Mass Spectrometry (MALDI-MS). A higher concentration of H_2O_2 (1% H_2O_2) was employed in this experiment to exploit a higher self-propulsion speed and enhanced photocatalytic activity required to break the strong covalent bonds in polymer chains. The sample was exposed to UV-light irradiation for 24 h in the presence of the cubic microrobots leading to the self-assembled microchains. **Figure 6b** reports MALDI spectra of bare PEG and microrobots-treated PEG solution. Signals corresponding to PEG macromolecular chains around 4000 mass completely disappeared after the treatment with microchains upon exposure to UV-light and H_2O_2, which is attributed to the combination of photocatalysis and catalyzed photo-Fenton reaction producing photogenerated ROS to attack C–O bonds in PEG backbone. [40]

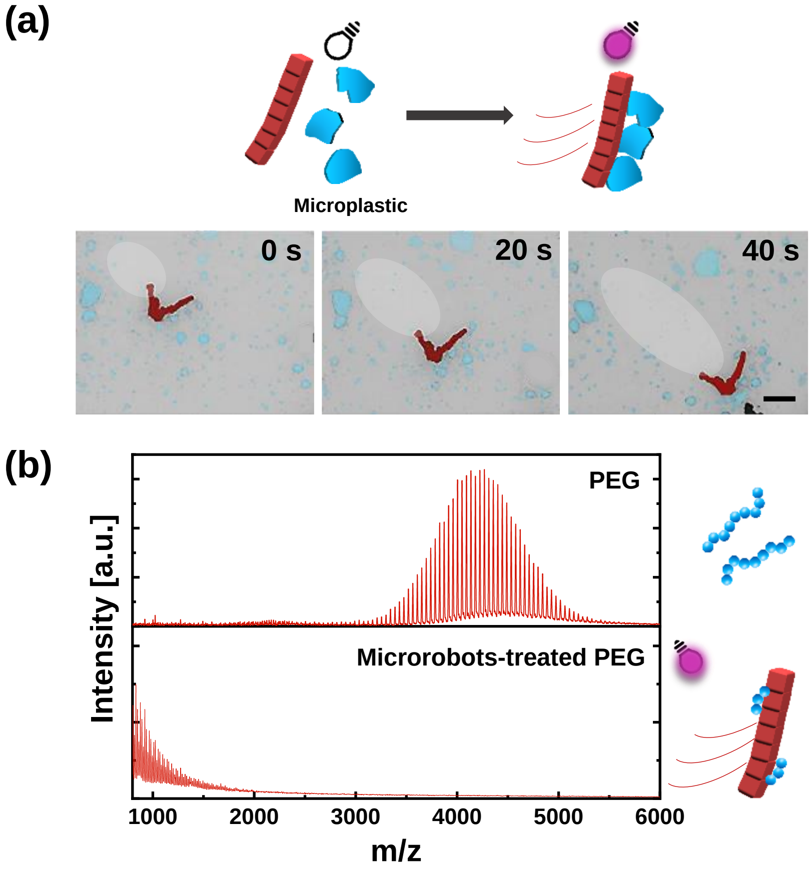

Figure 6. (a) Artificially colored time-lapse images of a self-assembled microchain for the removal of suspended matter under UV-light irradiation in 0.1% H_2O_2 (the white circles represent the area of suspended matter removal, blue areas are suspended matter pieces, red areas are microchains. Scale bar is 5 µm). (b) PEG chains photodegradation. From top to bottom, MALDI-MS of untreated PEG and PEG treated with microchains under 24 h UV-light irradiation in 1% H_2O_2.

Conclusion

In summary, we have demonstrated the influence of hematite/Pt microrobots shapes on their self-assembly behaviors. Because of the asymmetrical dipolar moment orientation in the crystal, cubic hematite/Pt microrobots can self-organize into regular microchains with morphologies remarkably different from those of walnut microrobots, which solely display random aggregation. Taking advantage of the intriguing collective behaviour, we also developed a novel light-powered microchains composed of individual cubic hematite/Pt microrobots, exhibiting autonomous locomotion under UV-light irradiation in presence of low concentration of H_2O_2. These microchains demonstrate different types of self-propulsion depending on the various possible mutual orientations of the microrobots during the self-assembly. To prove the exceptional benefits of a collective behavior compared to individual microrobot, these light-powered self-assembled microchains were employed for yeast cells capture, realease and transport, for the capture and removal of suspended matter in water originated from personal care products, as well as the definitive degradation of polymeric materials. This work offers a new perspective on the collective behavior of photocatalytic microrobots with the benefits of easily batch fabrication, low-cost, and broad range of applications.

Authors Contributions

X.P. performed the fabrication of the microrobots, recorded, and analyzed their motion, performed SEM-EDX analysis, Tafel measurements, carried out the cargo transportation experiments, and interpreted the data. M.Ur. designed the experiments, performed the numerical simulation, and contributed to data interpretation. M. Us. contributed to the degradation experiment and analyzed the data. M.P. originated the idea. M.P. and M.Ur. supervised the project. All authors contributed to writing the manuscript.

Acknowledgments

M.P. was supported by Ministry of Education, Youth and Sports (Czech Republic) grant LL2002 under the ERC CZ program. X.P. was supported by the China Scholarship Council (CSC No. 202008320382). M.Ur. acknowledges the financial support by the European Union's Horizon 2020 research and innovation program under the Marie Skłodowska-Curie grant agreement No. 101038066. CzechNanoLab project LM2018110 funded by MEYS CR is gratefully acknowledged for the financial support of the measurements/sample fabrication at CEITEC Nano Research Infrastructure.

References

[1] Jin, D.; Yu, J.; Yuan, K.; Zhang, L. Mimicking the Structure and Function of Ant Bridges in a Reconfigurable Microswarm for Electronic Applications. *ACS Nano* **2019**, *13*, 5999–6007.

[2] Garattoni, L.; Birattari, M. Autonomous Task Sequencing in a Robot Swarm. *Sci. Robot.* **2018**, *3*, 1–12.

[3] Rubenstein, M.; Cornejo, A.; Nagpal, R. Programmable Self-assembly in a Thousand-robot Swarm. **2014**, *345*, 795–800.

[4] Gao, W.; Sattayasamitsathit, S.; Wang, J. Catalytically Propelled Micro-/nanomotors: How Fast Can They Move? *Chem. Rec.* **2012**, *12*, 224–231.

[5] Wang, H.; Moo, J.; Pumera, M. From Nanomotors to Micromotors: The Influence of the Size of an Autonomous Bubble-Propelled Device upon Its Motion. *ACS Nano* **2016**, *10*, 5041–5050.

[6] Li, J.; Yu, X.; Xu, M.; Liu, W.; Sandraz, E.; Lan, H.; Wang, J.; Cohen, M. Metal-organic

Frameworks as Micromotors with Tunable Engines and Brakes. *J. Am. Chem. Soc.* **2017**, *139*, 611–614.

[7] Wang, Q.; Dong, R.; Wang, C.; Xu, S.; Chen, D.; Liang, Y.; Ren, B.; Gao, W.; Cai, Y. Glucose-Fueled Micromotors with Highly Efficient Visible-Light Photocatalytic Propulsion. *ACS Appl. Mater. Interfaces* **2019**, *11*, 6201−6207.

[8] Ma, X.; Wang, X.; Hahn, K.; Sánchez, S. Motion Control of Urea-Powered Biocompatible Hollow Microcapsules. *ACS Nano* **2016**, *10*, 3597–3605.

[9] Pourrahimi, A. M.; Villa, K.; Palenzuela, C. L.; Ying, Y.; Sofer, Z.; Pumera, M. Catalytic and Light-Driven ZnO/Pt Janus Nano/Micromotors: Switching of Motion Mechanism via Interface Roughness and Defect Tailoring at the Nanoscale. *Adv. Funct. Mater.* **2019**, *29*, 1–8.

[10] Lin, Z.; Fan, X.; Sun, M.; Gao, C.; He, Q.; Xie, H. Magnetically Actuated Peanut Colloid Motors for Cell Manipulation and Patterning. *ACS Nano* **2018**, *12*, 2539–2545.

[11] Xu, T.; Soto, F.; Gao, W.; Garcia-Gradilla, V.; Li, J.; Zhang, X.; Wang, J.; Ultrasound-modulated bubble propulsion of chemically powered microengines. *J. Am. Chem. Soc.* **2014**, *136*, 8552–8555.

[12] Urso, M.; Iffelsberger, C.; Mayorga-Martinez, C. C.; Pumera, M. Nickel Sulfide Microrockets as Self-Propelled Energy Storage Devices to Power Electronic Circuits ‘On-Demand. *Small Methods* **2021**, *2100511*, 1–9.

[13] Oral, C. M.; Ussia, M.; Pumera, M. Self-Propelled Activated Carbon Micromotors for ‘on-the-Fly’ Capture of Nitroaromatic Explosives. *J. Phys. Chem. C* **2021**, *125*, 18040–18045.

[14] Gao, W.; D'Agostino, M.; Garcia-Gradilla, V.; Orozco, J.; Wang, J. Multi-fuel Driven Janus Micromotors. *Small* **2013**, *9*, 467–471.

[15] Eskandarloo, H.; Kierulf, A.; Abbaspourrad, A. Light-harvesting Synthetic Nano- and Micromotors: A Review. *Nanoscale* **2017**, *9*, 12218–12230.

[16] Jurado-Sánchez, B.; Pacheco, M.; Maria-Hormigos, R.; Escarpa, A. Perspectives on Janus Micromotors: Materials and Applications. *Appl. Mater. Today* **2017**, *9*, 407–418.

[17] Jurado-Sánchez, B.; Pacheco, M.; Rojo, J.; Escarpa, A. Magnetocatalytic Graphene Quantum Dots Janus Micromotors for Bacterial Endotoxin Detection. *Angew. Chemie - Int. Ed.* **2017**, *56*, 6957–6961.

[18] Dong, R.; Zhang, Q.; Gao, W.; Pei, A.; Ren, B. Highly Efficient Light-Driven TiO_2−Au Janus Micromotors. *ACS Nano* **2016**, *10*, 839–844.

[19] Ussia, M.; Urso, M.; Dolezelikova, K.; Michalkova, H.; Adam, V.; Pumera, M. Active Light-Powered Antibiofilm ZnO Micromotors with Chemically Programmable Properties. *Adv. Funct. Mater.* **2021**, *2101178*, 1-10.

[20] Pourrahimi, A. M.; Villa, K.; Ying, Y.; Sofer, Z.; Pumera, M. ZnO/ZnO_2 /Pt Janus Micromotors Propulsion Mode Changes with Size and Interface Structure: Enhanced Nitroaromatic Explosives Degradation under Visible Light. *ACS Appl. Mater. Interfaces* **2018**, *10*, 42688–42697.

[21] Peng, X.; Zhu, H.; Chen, H.; Feng, X.; Liu, R.; Huang, Z.; Shen, Q.; Ma, Y.; Wang, L. Eco-friendly Porous Iron(iii) Oxide Micromotors for Efficient Wastewater Cleaning. *New J. Chem.* **2019**, *43*, 12594–12600.

[22] Urso, M.; Ussia, M.; Pumera, M. Breaking Polymer Chains with Self-Propelled Light-

Controlled Navigable Hematite Microrobots. *Adv. Funct. Mater.* **2021**, *2101510*, 1–10.

[23] Dong, R.; Hu, Y.; Wu, Y.; Gao, W.; Ren, B.; Wang, Q.; Cai, Y. Visible-Light-Driven BiOI-Based Janus Micromotor in Pure Water. *J. Am. Chem. Soc.* **2017**, *139*, 1722–1725.

[24] Xiao, Z.; Chen, J.; Duan, S.; Lv, X.; Wang, J.; Ma, X.; Tang, J.; Wang, W. Bimetallic Coatings Synergistically Enhance the Speeds of Photocatalytic TiO_2 Micromotors. *Chem. Commun.,* **2020**, *56*, 4728–4731.

[25] Maric, T.; Nasir, M. Z.; Webster, M. R. D.; Pumera, M. Tailoring Metal/TiO_2 Interface to Influence Motion of Light-Activated Janus Micromotors. *Adv. Funct. Mater.* **2020**, *1908614*, 1–6.

[26] Kong, L.; Rohaizad, N.; Nasir, M.; Guan, J.; Pumera, M. Micromotor-Assisted Human Serum Glucose Biosensing. *Anal. Chem.* **2019**, *91*, 5660–5666.

[27] Gao, W.; Dong, R.; Thamphiwatana, S.; Li, J.; Gao, W.; Zhang, L.; Wang, J. Artificial Micromotors in the Mouse's Stomach: A Step toward in Vivo Use of Synthetic Motors. *ACS Nano* **2015**, *9*, 117–123.

[28] Mayorga-Martinez, C; Zelenka, J.; Grmela, J.; Michalkova, H.; Ruml, T.; Mareš, J.; Pumera, M. Swarming Aqua Sperm Micromotors for Active Bacterial Biofilms Removal in Confined Spaces. *Adv. Sci.* **2021**, *2101301*, 1–7.

[29] Peng, X.; Urso, M.; Pumera, M. Photo-Fenton Degradation of Nitroaromatic Explosives by Light-Powered Hematite Microrobots: When Higher Speed Is Not What We Go For. *Small Methods* **2021**, *2100617*, 1–9.

[30] Lu, C.; Tang, Z. Advanced Inorganic Nanoarchitectures from Oriented Self-Assembly. *Adv. Mater.* **2016**, *28*, 1096–1108.

[31] Yan, J.; Bloom, M.; Bae, S. C.; Luijten, E.; Granick, S. Linking Synchronization to Self-assembly Using Magnetic Janus Colloids. *Nature* **2012**, *491*, 578–581.

[32] Yu, J.; Yang, L.; Zhang, L. Pattern Generation and Motion Control of a Vortex-like Paramagnetic Nanoparticle Swarm. *Int. J. Rob. Res.* **2018**, *37*, 912–930.

[33] Snezhko, A.; Aranson, I. S. Magnetic Manipulation of Self-assembled Colloidal Asters," *Nat. Mater.* **2011**, *10*, 698–703.

[34] Breen, T. L.; Tien, J.; Scott, R.; Hadzic, T.; Whitesides, G. M. Design and Self-Assembly of Open, Regular, 3D Mesostructures. *Science* **1999**, *284*, 948−951.

[35] Gobre, V. V.; Tkatchenko, A. Scaling Laws for Van Der Waals Interactions in Nanostructured Materials. *Nat. Commun.* **2013**, *4*, 2341.

[36] Miele, E.; Raj, S.; Baraissov, Z.; Král, P.; Mirsaidov, U. Dynamics of Templated Assembly of Nanoparticle Filaments within Nanochannels. *Adv. Mater.* **2017**, *29*, 1702682.

[37] Rossi, L.; Donaldson, J.; Meijer, J.; Petukhov, A.; Kleckner, D.; Kantorovich, S.; Irvine, W.; Philipsec, A.; Sacanna, S.; Self-organization in Dipolar Cube Fluids Constrained by Competing Anisotropies. *Soft Matter* **2018**, *14*, 1080–1087.

[38] Meijer J. M.; Rossi, L. Preparation, Properties, and Applications of Magnetic Hematite Microparticles. *Soft Matter* **2021**, *17*, 2354–2368.

[39] Villa, K.; Novotný, F.; Zelenka, J.; Browne, M. P.; Ruml, T.; Pumera, M. Visible-Light-Driven Single-Component $BiVO_4$ Micromotors with the Autonomous Ability for Capturing Microorganisms. *ACS Nano* **2019**, *13*, 8135–8145.

[40] Ussia, M.; Urso, M. Miritello, M.; Bruno, E.; Curcuruto, G.; Vitalini, D.; Condorelli, G.;

Cantarella, M.; Priviterab, V.; Carroccio, S. C. Hybrid Nickel-Free Graphene/Porphyrin Rings for Photodegradation of Emerging Pollutants in Water. *RSC Adv.* **2019**, *9*, 30182–30194.